# A multi-dimensional parametric study of variability in multi-phase flow dynamics during geologic CO$_2$ sequestration accelerated with machine learning

Hao Wu [a,c,*], Nicholas Lubbers [b], Hari S. Viswanathan [c], Ryan M. Pollyea [a]

[a] *Department of Geosciences, Virginia Polytechnic Institute and State University, Blacksburg, VA, USA*
[b] *Computer, Computational, and Statistical Sciences Division, Los Alamos National Laboratory, Los Alamos, NM, USA*
[c] *Earth and Environmental Sciences Division, Los Alamos National Laboratory, Los Alamos, NM, USA*

## HIGHLIGHTS

- During carbon sequestration, CO$_2$ migration is affected by so many uncertainties.
- Numerical simulations of multi-phase fluid dynamics are computational expensive.
- The combined effects of capillary pressure and relative permeability are explored.
- The application of Machine Learning provides a huge computational speed-up.
- Capillary pressure imposes important effect to CO$_2$ and fluid pressure distribution.

## ARTICLE INFO

## ABSTRACT

Successful geologic CO$_2$ storage projects depend on numerical simulations to predict reservoir performance during site selection, injection verification, and post-injection monitoring phases of the project. These numerical simulations solve non-linear sets of coupled partial differential equations, while accounting for multi-phase fluid dynamics on the basis of constitutive equations that are embedded into the solution scheme. As a consequence, individual simulations often require tens to hundreds of hours to complete on high-performance computing clusters. Moreover, laboratory experiments reveal that parametric functions for capillary pressure and relative permeability exhibit substantial variability, even within the same rock type. This combination of computational expense and wide-ranging parametric variability means that there remains substantial uncertainty in the behavior of multi-phase CO$_2$-water systems, particularly in the context of feedbacks between relative permeability and capillary pressure. To bridge this knowledge gap, we develop a novel workflow that utilizes physics-based numerical simulation to train an artificial neural network (ANN) emulator for interrogating the multivariate parameter space that governs both capillary pressure and relative permeability. With this approach, the ANN is trained to emulate both fluid pressure distribution and CO$_2$ saturation, which are then interrogated quantitatively to generate parametric response surface mappings with high-fidelity resolution. Results from this study initially show that capillary entry pressure is the dominant control on both CO$_2$ plume geometry and fluid pressure propagation when considering the combined effects of capillary pressure and relative permeability, particularly when phase interference is low and residual CO$_2$ saturation is high. Moreover, the ANN emulator provides tremendous computational speed-up by computing 2691 individual simulations in several minutes; whereas, the same simulation ensemble would have required ~3 years of simulation time using only physics-based simulation methods (25,000 times speed up).

---

* Corresponding author at: Computer, Computational, and Statistical Sciences Division, Los Alamos National Laboratory, Los Alamos, NM, USA.
 *E-mail address:* wuhao90@vt.edu (H. Wu).

# 1. Introduction

Anthropogenic $CO_2$ emissions are strongly implicated in increasing global temperatures, and carbon capture and sequestration (CCS) is considered as an engineering-based approach designed to reduce the total mass of atmospheric $CO_2$ releases from point source generators [1,2,3,4,5]. Many potential geological formations have been proposed for anthropogenic $CO_2$ emission storage [6,7,8]. Among them, deep brine aquifers are of special interest because of their widespread worldwide distribution [9] and large storage capacity [10]. A successful CCS project is dependent on whether or not the injected $CO_2$ can be stored in the reservoir safely over a long-time period, e.g., $10^3$–$10^4$ years [1,11].

During $CO_2$ injection and trapping processes, uncertainties associated with reservoir properties and geologic conditions affect the distribution and migration of $CO_2$. For example, reservoir PTX (pressure, temperature, composition) conditions affect the thermodynamics of $CO_2$ dissolution [12,6], which in turn affects the saturation state that governs $CO_2$ plume geometry through capillary pressure [13] and relative permeability [14,15] effects. In natural geologic systems, these phenomena are subject to substantial uncertainty, which affects not only the migration of $CO_2$ but also the fluid pressure perturbation [16]. As a result, the interactions between PTX-dependent fluid properties and multi-phase fluid dynamics require careful consideration during CCS project assessment. To understand the mechanisms affecting $CO_2$ migration, numerous laboratory and modeling studies have been done to quantitively characterize $CO_2$ behavior under different reservoir conditions [17,18,19,20,21]. Wu et al. [13] discovered the effect of substantial variability of capillary pressure measurements on supercritical $CO_2$ ($scCO_2$) migration, and how this variability influences $CO_2$ plume geometry in a sandstone reservoir. In Pollyea [14], the uncertainty of relative permeability effects was quantified in a basalt reservoir by performing numerical $CO_2$ injection simulations, and the results showed that the injection pressure accumulation and $CO_2$ plume geometry are strongly affected by relative permeability as well. In addition, Jayne et al. [12] found that thermodynamic effects during $CO_2$ migration may cause a warming front of up to 4 °C within the reservoir due to $CO_2$ dissolution, and that these temperature changes can be used as a thermal monitor for predicting $CO_2$ breakthrough.

The migration of $CO_2$ and fluid pressure in geologic formations may cause leakage through abandoned wells and structural features, e.g., faults and fractures. As a result, the leakage of $CO_2$ not only reduces the storage efficiency but may also contaminate groundwater resources in shallow aquifers [16]. In order to assess the efficiency of CCS projects prior to the construction, it is essential to estimate the risk profile and evaluate reservoir performance [22,23,24,25]. The National Risk Assessment Partnership (NRAP), a U.S. Department of Energy initiative, has been pursuing research on leakage risk and reservoir performance for carbon sequestration. Many studies focus on the monitoring of $CO_2$ saturation and pressure propagation within the reservoir during injection for leakage risk estimation. More importantly, fluid pressure and $CO_2$ saturation results can be used as inputs for the leakage estimation model to predict rates and volumes of $CO_2$ leakage [26,27]. For example, Zhang et al. [28] modeled the potential of fluid migration detection based on $CO_2$ saturation and pressure monitoring in the overlying seal layer, in which exists a high permeability zone. The results showed that pressure response resulting from $CO_2$ migration was detected up to 1650 m from the centroid of the high permeability zone in the sealing layer. In addition, the results from Jayne et al. [29] generated 50 stochastic permeability distributions in the basalt reservoir for $CO_2$ migration simulations. The results suggested that uncertainty in reservoir-scale permeability greatly impacts the accumulation and distribution of $CO_2$. Besides $CO_2$ saturation and pressure detection, Yang et al. [30] focused on groundwater pH as an index to monitor leakage detection because groundwater pH decreases due to $CO_2$ dissolution. The computed results showed that the probability of leakage detection is over 90% when the change in pH is bigger than 0.7.

Even though many laboratory and numerical studies have been done to study the migration mechanisms of $CO_2$ and pressure in the reservoirs [31,32,33,34], there are some disadvantages to these two methods. First, laboratory experiments are completed on core-scale rock samples, and upscaling laboratory results to field scale models gives rise to uncertainties [35,36,9]. In addition, even though some numerical studies present the effect of reservoir uncertainties on $CO_2$ migration, the physics-based simulations are complicated and computationally expensive [37]. Some studies have shown that reservoir-scale simulations require days to months of computer time [26,38]. For example, the ensemble of 50 3-D $CO_2$ injection models developed by Pollyea et al. [39] required more than 200 days of compute time, while utilizing 1024 computer processors per simulation (~4.9 M processor hours). As numerical simulations become increasingly complex, there is a demonstrable need to increase computational efficiency while retaining the most salient attributes of the underlying physics. In this study, we combine recent advances in machine learning simulation methods with physics-based ensemble simulation techniques to unlock previously inaccessible knowledge about interconnected feedbacks between relative permeability and capillary pressure during $CO_2$ sequestration in a synthetic reservoir.

# 2. Background

In recent years, machine learning (ML) has become an important tool for efficiently analyzing large amounts of data in a variety of fields. As high-fidelity data sets become increasingly available for applications in many areas, ML methods are becoming an important tool for analyzing these "big data" problems [40,41,42,43]. For example, Karpatne et al. [44] used different ML methods, such as multitask learning and multi-instance learning, to estimate the amount of forest cover across four states in Brazil. These ML techniques showed good results in terms of the forest area. Similarly, Marjanović et al. [45], tested the support vector machines (SVM) method for high-performance landslide susceptibility mapping processes. The SVM method outperformed decision trees and logistic regression methods in evaluation measurements, and it provided an application of machine learning method in landslide risk assessment. Among the most beneficial use of ML methods is to reduce the computational cost of analyzing complex parameter spaces. For example, Smith et al. [46] have applied neural networks to small organic molecules that span an immense space, so that the resulting models can predict the results of computationally intensive quantum–mechanical calculations at a much lower computational cost. For computational cost reduction in risk monitoring during CCS, Chen et al. [47] utilized multivariate adaptive regression splines to derive reduced order models from physics-based numerical simulations of $CO_2$ injection in a saline aquifer. These reduced order models provide new insights for effective monitoring approaches about $CO_2$ leakage with substantially less computational overhead than traditional multi-physics numerical simulations.

The success of ML application in the geosciences is an outgrowth of the big data revolution that is transforming geosciences from a data-poor field to one with a wide variety of high-fidelity, multi-dimensional datasets [48]. The growing data availability opens up exciting new opportunities for the application of machine learning methods to problems in geosciences [40,49,50]. The application of ML has shown outstanding performance in improving computational efficiency for subsurface simulations [51,52]. For example, Valera et al. [53] developed an alternative network reduction approach for fluid flow in a 3-D fracture-controlled fluid system by applying the ML method, and the computational time decreased from hours to seconds. This latter study underscores the tremendous advantage in the application of ML methods, which is the ability to rapidly process patterns of large-scale and/or high-dimensional datasets, while efficiently capturing complex relationships between data and identifying previously inaccessible research targets. Importantly, this process also decreases personnel costs

and improves performance and reproducibility in comparison to human analysts [48,51]. In subsurface fluid-flow reservoir simulations, the primary goal of ML applications is to make highly accurate predictions of fluid migration, while improving computational efficiency. In doing so, the purpose of supervised ML methods is to find a low-cost empirical model that can map all input properties to their corresponding output variables, thus allowing for rapid predictions across all possible combinations of input parameters. ML prediction should be considered as an expansion to physics-based simulations and not a replacement [54]. Some studies have shown the exploration of ML models in reservoir characterization. For example, Walls et al. [55] applied neural networks to predict lithologic classes based on the training of well log curves, e.g. total porosity, clay volume, and water saturation, in a North Sea turbidite. A 200 m depth interval of five well log data was used for training, and, afterward, the network was applied to expand the prediction of lithology to the full seismic volume ($\sim 5 \times 10^5$ km$^3$). This process is also characterized as supervised learning, which is widely applied to physics-based problems [52].

One widely used ML method is the artificial neural network (ANN) model, loosely based on simple models of interconnected biological neurons [56]. ANN algorithms, consisting of a set of neurons, aim to find a representation that maps input parameters to output variables [48]. ANN is widely used for capturing features of image data from large datasets and was shown excellent performance for reducing the dimensionality of data [57,58]. As a result, ANN models have become popular in the geosciences applications for modeling nonlinear relationships [48]. For example, Beucher et al. [59] described the application of an ANN model for acid sulfate (AS) soil mapping to classify AS soil and non-AS soil sites. In addition, DeVries et al. [38] accelerated the calculation of viscoelastic earthquake cycle activity by more than 50,000% applying extended ANN approach.

Monitoring the fluid flow migration mechanisms of CCS projects is critical to ensure CO$_2$ storage safety and efficiency. Physics-based, multiphase fluid flow models that account for thermodynamics of the CO$_2$-brine system are frequently applied to understand the site-scale behavior of CCS projects. For example, Wu et al. [13] and Pollyea [14] used response surface methods to gain insights into the effects of uncertainty in capillary pressure and relative permeability models, respectively, during industrial-scale CO$_2$ injections. However, in storage reservoirs, numerous physical properties affect CO$_2$ migration simultaneously. As a result, it is important to build a comprehensive understanding of CO$_2$ migration mechanisms under more realistic conditions. However, simulations that quantify realistic conditions of the fluid migration mechanism are computationally expensive and time consuming, requiring thousands of hours of computing time on a high-performance computing cluster. Recently, the application of ML has shown outstanding performance to speed up these simulations by capturing fundamental attributes, such as fluid pressure accumulation and CO$_2$ saturation distribution. The objective of this study is to constrain CO$_2$ plume geometry and fluid pressure perturbation during industrial-scale CO$_2$ sequestration in a synthetic sandstone reservoir, while taking into account joint parametric variability in both relative permeability and capillary pressure functions. In doing so, supervised ML using a deep ANN model is applied to capture the distribution of CO$_2$ saturation and fluid pressure. The ML training process is based on 460 physics-based simulations describing different combinations of capillary pressure and relative permeability parameters. Afterward, the CO$_2$ saturation and pressure migration under unknown capillary pressure and relative permeability conditions are explored. This study provides a better understanding of the increased computational efficiency of computational simulations of CO$_2$ sequestration achieved by ML application. In addition, the prediction results provide fundamental supports for future improvement in the siting process of CCS field reservoir applications.

## 3. Methods

### 3.1. Physical model

The conceptual model is a hypothetical sandstone reservoir that is (i) regionally confined by low permeability caprock, e.g., shale, and (ii) occurs at depth $\sim$2000 m, with 16 m thickness and 100 km lateral extent (Fig. 1). This model domain is a 3-D cylindrical volume, which is discretized as a 2-D system due to axial asymmetry. The injection well is completed in the center of the model domain with a radius of 0.1 m. Beyond the injection well, the model domain is discretized in the radial direction with 949 grid cells that increase logarithmically to a radial extent of 10,000 m. To simulate a semi-infinite far-field, the radial dimension is further discretized between 10,000 m and 100,000 m with 50 additional grid cells to ameliorate non-physical pressure feedbacks from the lateral boundary. Vertical grid discretization is 1 m. The upper and lower boundaries are specified as adiabatic (no flow) because CCS reservoirs are generally confined by low permeability shale formations. The centrally located injection well is a Neumann type boundary, where CO$_2$ is being injected through injection well at a constant rate of 8.0 kg/s for ten years. Initial conditions are specified as fully saturated in the wetting phase, with fluid pressure of 20 MPa, and temperature of 75 °C. These conditions reflect a disposal reservoir at $\sim$2 km depth, where injected CO$_2$ exists as a supercritical phase fluid (scCO$_2$). The hydraulic parameters are listed in Table 1 based on Berea sandstone [60].

In this study, the effects of capillary pressure and relative permeability on CO$_2$ migration mechanisms in storage reservoirs are modeled using characteristic curves, i.e., constitutive models. Capillary pressure effects are calculated using the constitutive relation originally developed by van Genuchten [61], which models capillary pressure as a function of effective wetting phase saturation ($S^*$) through the equation:

$$P_{cap} = -P_o \left( [S^*]^{-\frac{1}{\lambda}} - 1 \right)^{1-\lambda}. \tag{1}$$

In Equation (1), $P_o$ is the entry pressure, which characterizes the pressure increment required for the gas phase to first enters the pore network, $\lambda$ is a fitting parameter (commonly called the phase interference parameter), which controls the curvature of the model, and $S^*$ is the effective wetting phase saturation, which is calculated as:

$$S^* = \frac{S_l - S_{lr}}{S_{ls} - S_{lr}}. \tag{2}$$

In Equation (2), $S_l$ is wetting phase saturation, $S_{lr}$ is the residual wetting phase saturation, and $S_{ls}$ is the saturated wetting phase saturation. These end member saturations represent conditions when (i) the wetting-phase is fully mobile ($S_{ls}$) and (ii) the wetting phase is immobile ($S_{lr}$). For this study, $S_{ls}$ and $S_{lr}$ are unity and 0.3, respectively.

Wetting phase relative permeability is calculated with the van Genuchten-Mualem model [61], and it is given as:

$$k_w = \sqrt{S^*} \left[ 1 - \left( 1 - S^{*\frac{1}{\lambda}} \right)^{\lambda} \right]^2, \tag{3}$$

where $\lambda$ is van Genuchten fitting parameter, and $S^*$ is the effective wetting phase saturation (Eq. (2)). Non-wetting phase relative permeability is calculated with Corey curve [62] as:

$$k_{nw} = \left( 1 - \widehat{S} \right)^2 \left( 1 - \widehat{S}^2 \right), \tag{4}$$

where $\widehat{S}$ is effective non-wetting phase saturation, and is represented as:

$$\widehat{S} = \frac{S_l - S_{lr}}{1 - S_{lr} - S_{gr}}. \tag{5}$$

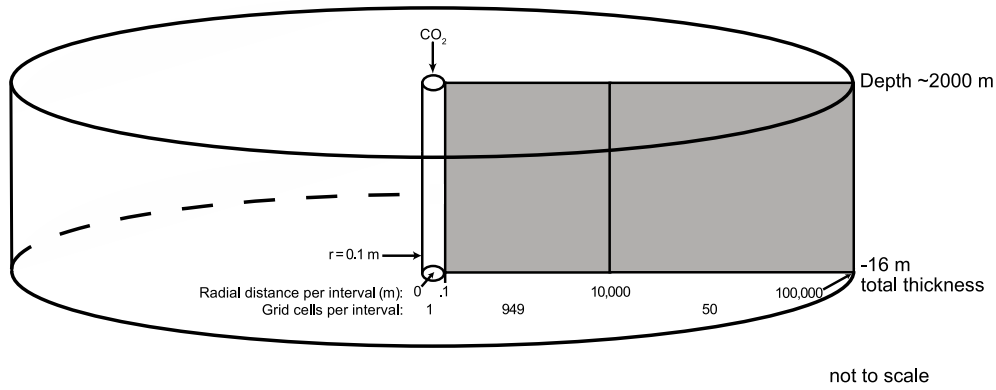In Equation (5), $S_l$, and $S_{lr}$ are wetting phase saturation and residual

**Fig. 1.** Two-dimensional symmetric model domain used in this study. The injection well is completed in the domain center with 0.1 m radius, and the next 949 grid cells with logarithmically increasing to 10,000 m, after which 50 grid cells increasing logarithmically to 100,000 m. The thickness of this domain is 16 m with a constant 1 m grid cell interval. Supercritical $CO_2$ is being injected through the injection well at a rate of 8.0 kg/s (252,461 MT/year) for 10 years.

**Table 1**
Bulk hydrogeology and thermal reservoir properties.

| Reservoir properties | | | |
|---|---|---|---|
| Property | Symbol | Value | Units |
| Fluid Pressure | $P_f$ | 20 | MPa |
| Temperature | T | 75 | °C |
| Salinity | $C_{NaCl}$ | 10,000 | ppm |
| Permeability | k | $4 \times 10^{-13}$ | m$^2$ |
| Porosity | $\phi$ | 0.2 | – |
| Density | $\rho_r$ | 2038 | kg m$^{-3}$ |
| Specific heat | $C_p$ | 1000 | J (kg K)$^{-1}$ |
| Thermal conductivity | $\kappa_r$ | 1.6 | W (m K)$^{-1}$ |



**Fig. 2.** 3-D parameter combination distribution for datasets. Phase interference parameter $\lambda$ governs curvature of van Genuchten model, while entry Pressure $P_o$ characterizes the pressure drop across the interface, and Residual gas saturation $S_{gr}$ is the residual gas phase ($CO_2$) saturation. 460 of different parameter combinations are randomly distributed in the parameter space, which consists of three sub-datasets. The amount of data for training, validation, and testing dataset are 340, 70, and 50, respectively.

wetting phase saturation (Eq. (2)), and $S_{gr}$ is residual non-wetting phase saturation when fully immobile. In this formulation for relative permeability, $S_{gr}$ governs curvature of the non-wetting phase relative permeability model (Eq. (4)) and $\lambda$ controls the curvature of the wetting-phase relative permeability model (Eq. (3)).

As shown in Pollyea [14] and Wu et al. [13], $P_o$, $\lambda$, and $S_{gr}$ are important parameters controlling the geometry of $CO_2$ plume and corresponding fluid pressure distribution during the $CO_2$ injection period; however, these parameters are subject to substantial uncertainty at the reservoir-site scale. Thus, the focus of this study is to quantify the role of these three parameters on $CO_2$ migration and pressure distribution. The ranges for $P_o$, $\lambda$, and $S_{gr}$ are 1–200 kPa, 0.4–0.8, and 0.1–0.4, respectively [15,36,60,63,64,65,6,66,67,68]. In this study, $\lambda$ is the same parameter in capillary pressure and relative permeability model. Different capillary pressure and relative permeability models are defined by different parameter combinations of $P_o$, $\lambda$, and $S_{gr}$.

To explain the effects of capillary pressure and relative permeability, a simulation ensemble is produced for unique combinations of $P_o$, $\lambda$, and $S_{gr}$ (from $P_{cap}$ and $k_{rel}$ model). The simulation ensemble is then analyzed to quantify the variability in both $CO_2$ migration and fluid pressure perturbation during $CO_2$ injections in a sandstone reservoir. A total of 460 different parameter combinations are randomly selected from the 3-D parameter space (Fig. 2), and simulations are completed using TOUGH3 [69], compiled with the fluid property module, ECO2N [70]. The TOUGH3/ECO2N simulation code models nonisothermal mixtures of $CO_2$, brine, and water using the multi-phase formulation for Darcy's Law with phase partitioning on the basis of local equilibrium. Results from the physics-based simulation ensemble are utilized to train the ANN model, which is designed to provide estimates of both $CO_2$ plume geometry and fluid pressure propagation for unsampled portions of the 3-D parameter space.
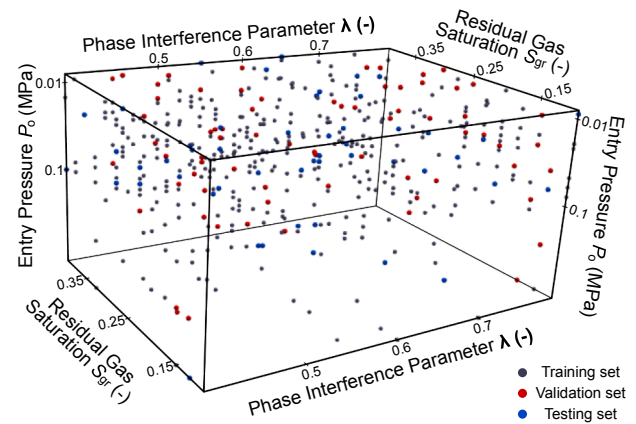
### 3.2. Artificial neuron networks (ANN)

The ANN model is widely used in geosciences to analyze large datasets (i.e., "big data" problems) and it has been tested to be highly effective for capturing features of image data with large variabilities. The basic unit of a neural network is the neuron, and each neuron comprises a simple function. Each neuron has the same functional form but with independently variable learnable parameters [71]. Layers in ANN are characterized as different combinations of a specified number of neurons, where the calculated information is transferred between different layers, and ANN are composed of several different layers.

Each neuron is an algorithm, which maps the relationship between inputs and outputs. The functional form of a single neuron is given by a set of weights and biases, along with an activation function, which are used to compute the activation (output) of a neuron as,

$$a = f\left( \sum_i^N \omega_i x_i + b_i \right),$$

where $x$, $a$, $\omega$, and $b$ represent input, output, weight, and bias, respectively, $f$ is the specific activation function, and $N$ is the total number of inputs. Typically, $\omega$ and $b$ are unique to each neuron. The structure of ANN is described as many interconnected neurons organized as parallel

layers (Fig. 3). For this study, the first layer corresponds to the input layer comprising five neurons, which are three parameters ($P_o$, $\lambda$, $S_{gr}$) and spatial two coordinates (lateral and vertical) of each location. The last layer (the "output layer") of the network constitutes the model predictions, which in this study is a single neuron that describes either $CO_2$ saturation (sat) or pressure change ($\Delta P$) for the given input location and simulation parameters. The interior layers are referred to as "hidden layers" to transfer inputs and outputs [38].

Inside the ANN, neurons take a weighted linear combination of the previous layer values and calculate a single value for the next layer by applying a specific function (Fig. 3). More specifically, $a_1^{l-1}, a_2^{l-1}, \cdots.. a_N^{l-1}$ are outputs of $l-1$ layer. For neuron $i$ in layer $l$, $a_i^l = f(\sum w_i a_i^{l-1} + b_i)$ is calculated by taking values from the previous layer as input, and it outputs a single value to every neuron in layer $l+1$ [72]. For $CO_2$ saturation, which ranges from 0 to 1, we choose the sigmoidal activation for the output neuron. For pressure perturbation, which has no pre-defined range, we choose the linear activation function. As activations are computed in a single forward direction, the network is characterized as a *feedforward* network. Meanwhile, when dealing with different data, researchers should also take the structure of the network into account, which is specified by the number of neurons per layer and the number of hidden layers. In this study, separate deep ANN structures are utilized in training $CO_2$ saturation and pressure: for pressure perturbation training, 40 neurons per layer and 3 hidden layers were used, while for $CO_2$ saturation training, a deeper structure of 60 neurons per layer and 4 hidden layers were applied. These values were found via hyper-parameter search on the validation data, exploring layer widths of 20, 40, and 60 neurons and depths of 2, 3, 4 layers.

The workflow of ANN consists of two phases: network training and final performance estimate (Fig. 4). These two phases require datasets for training, validation, and testing. The aggregate of these three data-sets constitute the full dataset required for developing the ANN emulator. Each dataset consists of two parts: five input parameters and the physics-based simulation results (Section 2.1). The training dataset is used for capturing features of simulation results, and the ML model calculates predictions based on the captured features. For evaluation, a cost function, the mean squared error (MSE), is applied to compare the
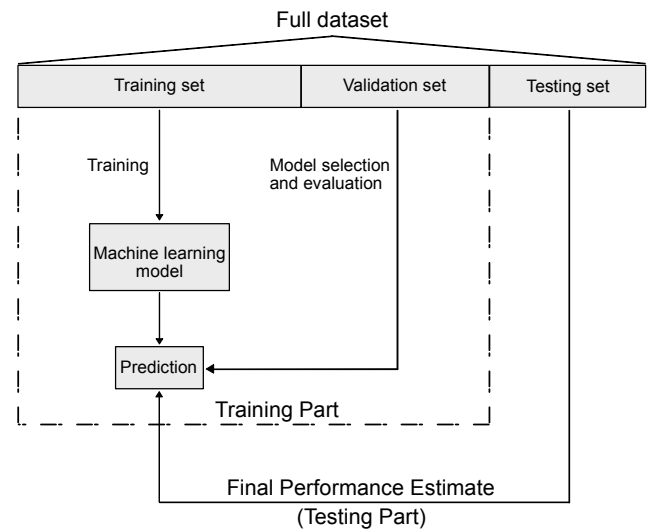


**Fig. 4.** Workflow of artificial neuron networks (ANN). There are two phases of ANN: training phase and test phase, and the full dataset consists of training set, validation set, and testing set throughout the two phases. The training set is applied to the machine learning model for features capture, and parameters of the machine learning model are updated through evaluation. The validation set is applied for model selection and evaluation. During phase two, the testing set is used for prediction performance evaluation.

physics-bases results and the results predicted by the ANN. The ANN model is trained by minimizing the cost function by gradient descent over batches of the dataset. The training phase processes many epochs, which is one complete presentation of the data set to be learned by ANN model, to capture features of physics-based results. During training, each epoch consists of exposing the network to a batch of samples to produce the predicted values and the cost function, then computing the gradient of network parameters (weights and biases), where the Adam [73] variant of gradient descent was applied. After one batch, this process is repeated for further batches of examples until the entire
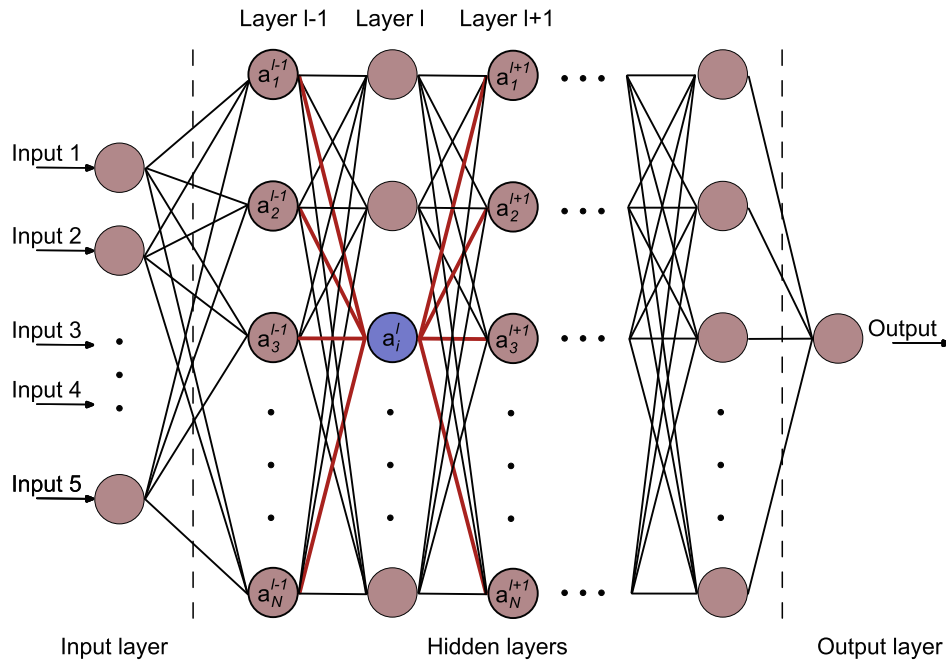


**Fig. 3.** Structure and setup of an example of artificial neuron networks (ANN). ANN consist of input layer, output layer, and hidden layers. Inside ANN, neurons representing weights take a weighted linear combination of the previous layer values and calculate a single value for the next layer applying a specific function. In this study, five neurons in the input layer correspond to five input parameters, and one neuron of the output layer represents the $CO_2$ saturation or pressure output.

dataset has been presented to the network. Afterward, these computed parameters are updated with respect to that gradient through the whole network. At the same time, after each epoch, the validation dataset is used to evaluate the model after the training of the training set, especially to avoid overfitting on the training set, and this process improves the accuracy of prediction. Overfitting denotes a setback during training, in which the ML model is emphasizing or memorizing some certain parts of the dataset, resulting in improvements on the training dataset which do not generalize, as signaled by the performance on the validation dataset. To avoid overfitting, early stopping is performed, in

which training is stopped if the validation error does not improve for 200 epochs, and the model is reverted to the parameter set which performed best on the validation data. After the whole training process, the performance of prediction through the trained ML model is tested on the testing dataset in the final performance estimate step.

To explore the combined effects of capillary pressure and relative permeability, a 3-D parameter space comprising $P_o$, $\lambda$, and $S_{gr}$ is created to identify systematic changes in $CO_2$ plume geometry and fluid pressure propagation on the basis of these three reservoir properties (Fig. 2). Each point in this parameter space represents a unique combination $P_o$, $\lambda$, and
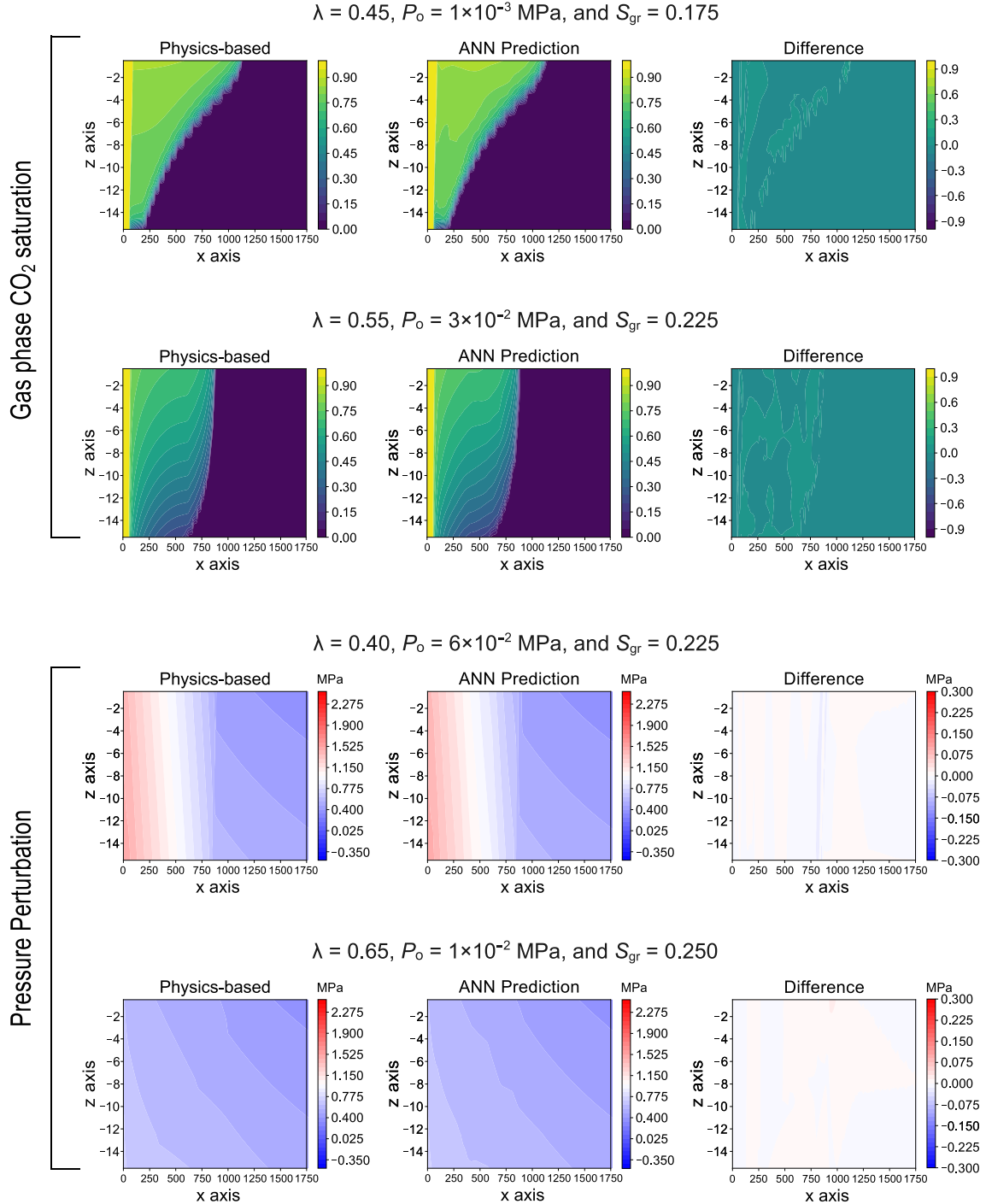


**Fig. 5.** ANN Prediction results analyses of four different capillary pressure and relative permeability parameter combinations for $CO_2$ saturation and fluid pressure perturbation. From left to right, the figures demonstrate the physics-based simulation results, ANN prediction results, and the difference between them. The color scale for the pressure perturbation difference plots is zoomed-in compared to the simulation and prediction results.

$S_{gr}$. The full dataset for ANN training, validation and testing comprises $CO_2$ saturation and fluid pressure results from the physics-based numerical simulations of 460 randomly selected parameter combinations. The full dataset is segmented in 340 for ANN training, 70 for ANN validation, and 50 for ANN testing. The ANN emulator is developed using the Pytorch deep learning library [74].

## 4. Results & discussion

### 4.1. Overall accuracy

The ANN training process captures features of physics-based simulation results, and then stops when no further improvement of the cost function is achieved. Once the training process is finished, prediction for the whole testing dataset is made based on the best ML model found through training. The results and analyses of the prediction of the testing dataset are shown in Figs. 5 and 6. All the figures show the results at the end of 10 years' injection time.

In Fig. 5, four different parameters combinations of capillary pressure and relative permeability models ($P_o$, $\lambda$, and $S_{gr}$) are represented to analyze accuracy of ANN model prediction for $CO_2$ saturation and pressure perturbation. An additional ten randomly selected parameter combinations of the testing dataset are shown in Appendix Figs. S1 and S2 for $CO_2$ saturation and pressure, respectively. From left to right, the figures demonstrate the physics-based simulation results, ANN prediction results, and the difference between them. The broad similarity between the physical and predicted images implies that the ANN model captures the salient aspects of the physics-based model.

Fig. 6 shows the complete evaluation of prediction results for $CO_2$ saturation and pressure accumulation across the reservoir for all 50

simulation results in the testing dataset. Fig. 6A, 6D illustrate the ANN results in comparison with physics-based results for each grid cell of the reservoir domain for the whole testing dataset, which is a 50-simulation ensemble. For this analysis, the dots are colored by the number of grid cells that correspond with the physics-ANN comparison. Note that the red diagonal denotes a perfect match, where physics-based results values are equal to ANN predicted values. The generally efficacy of the ANN emulator is apparent as counts exceed $10^4$ along the diagonal. As with the individual examples presented in Fig. 5, the aggregate analysis of ANN prediction shows that pressure perturbation (Fig. 6D) outperforms that for $CO_2$ saturation (Fig. 6A), as the pressure results precisely falling on the diagonal red line, whereas a number of the counted grid cells in the $CO_2$ saturation prediction scenario fall off the diagonal owing to the two steep leading edges of the $CO_2$ plume (Fig. 6A). The first steep edge is a large saturation drop around the injection well, across a fully saturated area (left yellow column in physics-based images of $CO_2$ saturation in Fig. 5). On top of this full saturation edge, the edge of the $CO_2$ plume also shows a steep saturation drop, ranging from non-zero to zero values. A similar situation was observed by Zhang et al. [28], who found that a steep saturation drop at the edge of $CO_2$ plume from ~0.1 to 0 at a short distance of 200 m. This systematic disparity occurs because the ANN model tends to smooth sharp gradients with more continuous changes. This phenomenon is a result of the $CO_2$ saturation requiring a deeper network to capture the boundary features in comparison to the fluid pressure. In addition, two peaks of the counted grid cell distribution are located in two corners where the saturation is 0% (bottom left of Fig. 6A) and 100% (top right of Fig. 6A), with a large number of grid cells falling in the area of 0% (no $CO_2$ saturation in the far-field) and 100% saturation (fully saturated around the injection well) area.
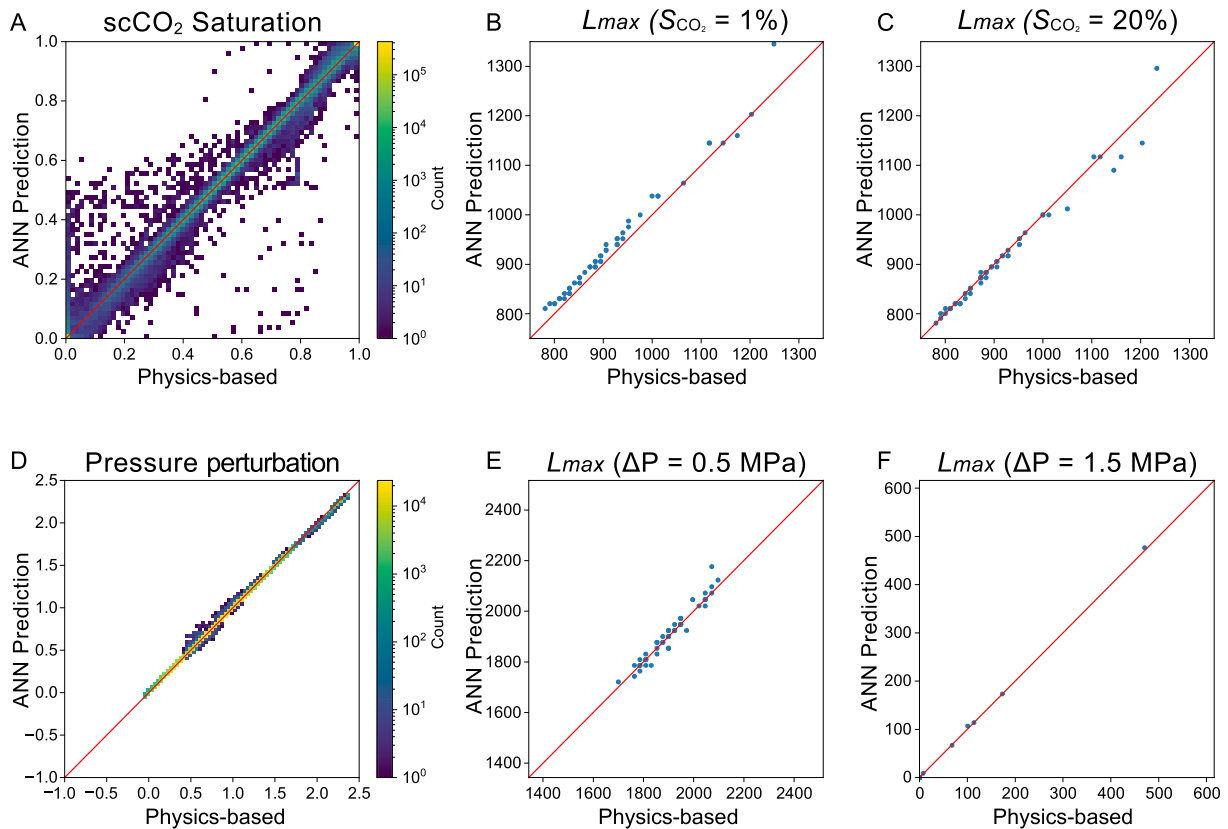


**Fig. 6.** The evaluation of predicted results for $CO_2$ saturation and pressure accumulation across the reservoir. Figures A and D illustrate the counted distribution of all grid cells in the testing dataset with the comparison between physics-based simulation and ANN prediction results of the reservoir domain. Figures B and C indicate the comparison of the maximal plume length when sat = 1% and 20% of physics-based and ANN prediction results for the testing dataset, respectively. Figures E and F demonstrate the lengths of pressure perturbation distribution when $\Delta P = 0.5$ MPa and 1.5 MPa for testing dataset, respectively.

The length of $CO_2$ saturation and pressure plume are of particular interest because they provide estimations for leakage observation and storage efficiency [26]. Fig. 6B presents the comparison between the physics-based and ANN prediction results for the testing dataset on the maximum length of the plume when $CO_2$ saturation is 0.01 (i.e., 1% free-phase $CO_2$), which is considered as the boundary of the plume. In contrast, Fig. 6C captures the plume migration maximal distance when $CO_2$ saturation is 0.2 (20% free-phase $CO_2$). The testing performance for the 20% $CO_2$ contour is better than that of the 1%, as indicated by a higher proportion of the 20% results falling on the diagonal. The reason for the performance difference lies in the smooth trend of ANN model at the plume boundary for 0.01 $CO_2$ saturation, which is harder to predict the steep drop of at the plume boundary for 0.01 $CO_2$ saturation. Similarly, Fig. 6E and 6F demonstrate the maximum length of pressure perturbation distribution when $\Delta P$ is 0.5 MPa and 1.5 MPa for testing dataset, respectively. The results imply that the trained ANN model performs well regarding pressure change. However, some physics-based simulations did not reach 1.5 MPa overpressure, resulting in fewer dots (counted grid cells with physics-ANN comparison) in Fig. 6F.

The results over the testing dataset demonstrate ANN emulation methods provide excellent results for capturing the major distribution of both $CO_2$ saturation and fluid pressure change when trained on physics-based numerical simulations. This result is well supported when comparing the pixel-by-pixel difference between the physics-based model and the ANN emulator (Fig. 5, third column). These results also show that much of the difference between the physics-based and ANN model occurs in predictions of $CO_2$ saturation at the leading edge of the plume, where the saturation gradient is the highest. In contrast, the differences in fluid pressure accumulation are more evenly distributed across the model. This disparity may be a result of the physical and chemical processes governing $CO_2$ migration and fluid pressure propagation. For example, fluid pressure propagation is governed by pressure diffusion, which is a smoothly varying response to the pressure gradient. In contrast, $CO_2$ saturation at the leading edge of the plume is governed by complex interactions between multi-phase transport properties and fluid system thermodynamics, i.e., $CO_2$ dissolution [12]. In aggregate, the individual results presented in Fig. 5 suggest that ANN methods adequately capture the overall patterns for both $CO_2$ saturation and fluid pressure propagation, but subtle variations of interconnected physical and chemical process are subject to modest uncertainty. How precisely the ANN model captures the location of the leading edge of the $CO_2$ plume is treated as a standard to decide the possibility of the ANN model. Enlarging the size of the training dataset is an optimal approach to improve training performance. Different sizes of the training dataset (50, 200, and 340) have been tested to demonstrate the adequate amount of the training data to be applied in the ANN model. In Fig. S3, it presents the pixel-by-pixel comparison between physics-based results and ANN results and the comparison about the maximum length of the plume of 1% and 20% $CO_2$ saturation for the testing dataset with different amount of training data (similar as Fig. 6). The comparison results proved that increasing the size of the training dataset enhances the training performance, and the model with 340 training data shows the best testing results in terms of better distribution along the red diagonal. Nonetheless, the performance of the model trained to 50 points was qualitatively correct, though it fails to accurately capture subtle measurements such as the plume length defined by a 1% saturation threshold. Increasing the size of the training dataset is able to get more accurate results [75], and it improves the reliability of the ANN model and provides more trustful predictions, which can be used in the latter analyses and field project applications. As a result, the 3-D prediction generations in the following section are based on the model with 340 training data.

### 4.2. Parametric analysis of 3-D parameter space

The ability of the ANN model to emulate results of the physics-based model suggests that the ANN model is suitable for sampling the parameter space at higher resolution with much greater computational efficiency than the physics-based modeling approach. On this basis, the ANN network developed in Section 2.2 is used to generate $CO_2$ saturation and pressure propagation models across a finely discretized sampling of the parameter space comprising 2691 unique parameter combinations. These ANN models are then utilized to generate response surface mappings for analyzing systematic variations of $CO_2$ plume geometry and pressure accumulation across the complete 3-D parameter space. Fig. 7A presents the complete response mapping for maximum lateral extent of 1% $CO_2$ saturation, which shows where the farthest plume edge (1% $CO_2$ saturation is treated as plume edge) is under different parameter combinations. To more clearly identify patterns in the response mapping, Fig. 7B presents an isosurface of Fig. 7A to illustrates the parameter combinations for which the maximum radial extent of 1% $CO_2$ saturation is 900 m: to find out under which parameter combinations, the farthest plume edge is 900 m. Similarly, Fig. 8A shows the response surface mappings for the maximum lateral extent of 0.5 MPa fluid pressure for ANN model (shows where the farthest 0.5 MPa pressure change edge is under different parameter combinations), while Fig. 8B shows the isosurfaces within Fig. 8A for which the maximum radial extent of 0.5 MPa fluid pressure propagation is 2000 m: to find out under which parameter combinations, the farthest 0.5 MPa pressure change edge is 2000 m.

The results of discrete analysis developed as part of the ANN testing procedure (Fig. 6A–C) illustrate the high efficiency of ANN predictions due to the comparison between physics-based results and ANN prediction results, and it provides support for detailed analysis of the ANN response and isosurface mappings across the completed 3-D parameter space. The prediction results provide a more comprehensive understanding of parameter effects analyses.

The results presented in Fig. 7 indicate that capillary entry pressure ($P_o$) imposes first-order control on the maximum extent of $CO_2$ migration. This is evident by the steep vertical gradient in the response map, particularly at low $P_o$ (Fig. 7A), as well as the 900 m isosurface, which exhibits a systematic trend across the parameter space (Fig. 7B). This result suggests that capillary pressure effects are more important for lateral $CO_2$ migration than relative permeability effects. This result contradicts Pollyea [14], which tested only the relative permeability parameter space found that $CO_2$ mobility, and thus plume extent, is governed by non-wetting phase relative permeability, which is largely controlled by residual gas saturation ($S_{gr}$). However, the finding that low entry pressure results in larger $CO_2$ plumes is congruent with Wu et al. [13], which tested the parameter space for the capillary pressure model. This phenomenon occurs because small $P_o$ encourages the migration of $CO_2$ saturation, however, the effects of $S_{gr}$ and $\lambda$ impose greater control on $CO_2$ plume extent as $P_o$ increases. This can be seen in Fig. 7B as the isosurface declines from back top left to front bottom right, where large $\lambda$ and small $S_{gr}$ facilitate increasing $CO_2$ mobility. These second order effects occur because phase interference ($\lambda$) governs the curvature of the wetting phase relative permeability, so that large $\lambda$ maintains greater wetting-phase relative permeability allowing (i) pore drainage to more readily occur and (ii) the $CO_2$ plume to migrate further from the injection well. In contrast, residual $CO_2$ saturation ($S_{gr}$) controls the curvature of non-wetting phase relative permeability, where large $S_{gr}$ results in dramatic changes to nonwetting-phase relative permeability for very small changes in wetting phase saturation. As a consequence, $S_{gr}$ is an important factor on $CO_2$ mobility, and small $S_{gr}$ maintains greater $CO_2$ mobility over a wider range of wetting phase saturation conditions. In aggregate, the black arrow on Fig. 7B indicates the curving trend of the isosurface taking the three parameters into account, however, the length of the $CO_2$ plume is inversely proportional to the declining trend of the isosurface. Generally, the length of the plume shows the largest values at low $P_o$, low $S_{gr}$, and high $\lambda$ (Fig. 7A, red circle) and the smallest values at high $P_o$, high $S_{gr}$, and low $\lambda$ (Fig. 7A, blue circle). To illustrate the variable effects of $S_{gr}$ with decreasing $\lambda$, two black dashed lines are drawn in
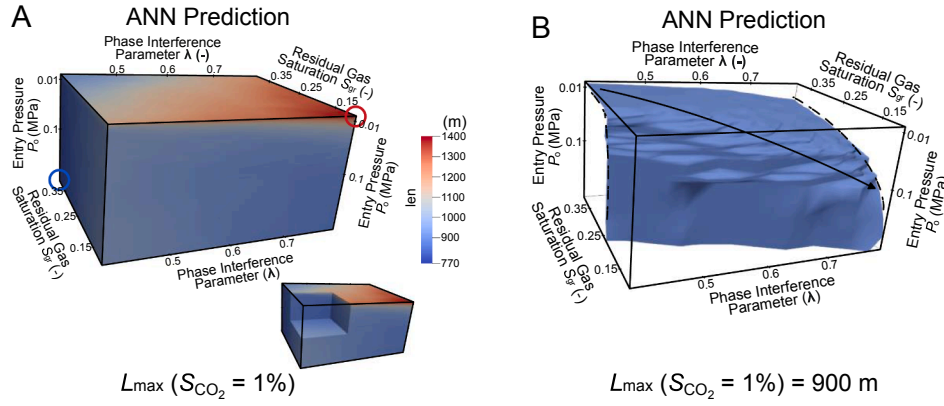
**Fig. 7.** Fig. A shows $CO_2$ saturation maximal expansion when sat = 1% over the 3-D parameter space for ANN prediction results. Inset illustrates cutaway for the interior structures of 3-D results. Fig. B shows the furthest plume edge (isosurfaces) of $CO_2$ saturation at 900 m when sat = 1% for ANN prediction results.
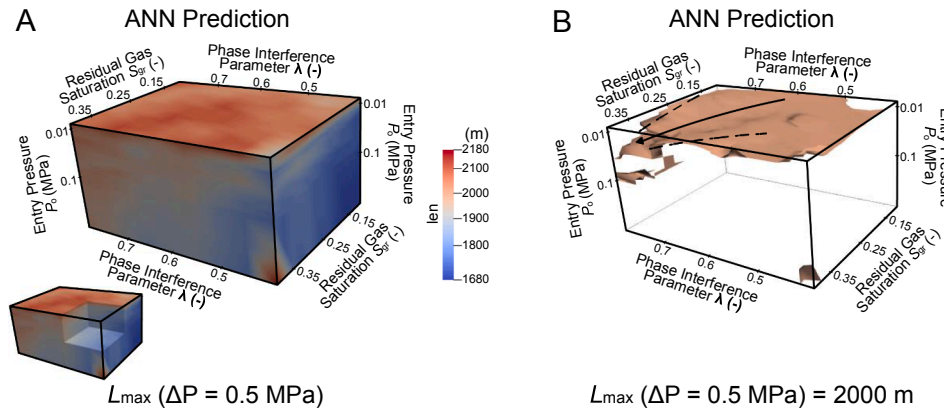


**Fig. 8.** Fig. A shows fluid pressure perturbation maximal expansion when ΔP = 0.5 MPa over the 3-D parameter space for ANN prediction results. Inset illustrates cutaway for the interior structures of 3-D results. The front side of the parameter domain in pressure is different from that in saturation figures (Fig. 4.7). Fig. B shows the furthest plume edge (isosurfaces) of fluid pressure perturbation at 2000 m when ΔP = 0.5 MPa for ANN prediction results.

Fig. 7B to show how the 900 m isosurface dips gently in the upper left (low $P_o$, low λ, and high $S_{gr}$), but the dips more steeply towards the lower right (high $P_o$, high λ, and low $S_{gr}$).

As with the $CO_2$ plume extent, $P_o$ is the dominant parameter for pressure perturbation, which is indicated by the almost horizontally distributed isosurfaces (Fig. 8B). Entry pressure is the largest control of $CO_2$ intrusion into pores media, and small $P_o$ implies more $CO_2$ intrusion and farther fluid pressure propagation. For high $P_o$, however, the effects of $S_{gr}$ and λ are not uniform. In low λ and low $S_{gr}$ area, their effect on fluid pressure propagation is limited, and $P_o$ controls the migration of fluid pressure. In contrast, high λ and high $S_{gr}$ encourage the migration of fluid pressure, supported by the declining trend of isosurface as shown in black arrow (Fig. 8B). In addition, λ and $S_{gr}$ show equal contribution to the increase of fluid pressure propagation, as indicated by the same slope of the two black dash lines (Fig. 8B). Specifically, there is a peak of fluid pressure propagation for high $S_{gr}$ and low λ, and this suggests that $S_{gr}$ imposes second-order control on pressure migration. $S_{gr}$ governs the mobility of the non-wetting phase, and high $S_{gr}$ illustrates the slow $CO_2$ mobility increase as it enters pores, resulting in the fast accumulation of fluid pressure.

The predicted results based on the ANN model provide an understanding of the combined effects of capillary pressure and relative permeability to $CO_2$ saturation and fluid pressure migration in a sandstone reservoir during the CCS injection period. Three parameters $P_o$, λ, and $S_{gr}$ from different capillary pressure and relative permeability models are studied, and the response surface results of 3-D parameter space show that $P_o$ is the dominant parameter controlling the migration

of $CO_2$ saturation and fluid pressure accumulation, which further implies that capillary pressure effects are of greater importance for predicting both $CO_2$ plume geometry and fluid pressure accumulation. Small $P_o$ encourages the migration of $CO_2$ saturation and fluid pressure accumulation, while large $P_o$ inhibits the migration. In addition, the effect of λ and $S_{gr}$ increase with increasing $P_o$. For $CO_2$ saturation, large λ and small $S_{gr}$ encourages the migration of $CO_2$ saturation, while the effect of $S_{gr}$ increases for the low λ range. However, high $S_{gr}$ encourages the migration of pressure to a large extent comparing to λ.

### 4.3. Applications of ML methods in CCS

To ensure $CO_2$ storage safety and efficiency, it is essential to monitor the fluid flow migration in CCS storage reservoirs. Many physics-based multi-phase fluid flow models accounting for different reservoir properties are applied to understand reservoir behaviors of CCS projects. In physics-based simulations, usually one single reservoir property with a large parametric variance is discussed for understanding its uncertainty effects to the multi-phase fluid flow system, e.g. relative permeability, capillary pressure, and thermal conductivity. However, it is computationally expensive and time consuming to quantify the simultaneous effects of more than one reservoir properties applying physics-based simulations. The application of ML method offers a substantial advantage for speeding up these simulations and makes it possible that to analyze the effects of parametric variability in higher dimensional space, e.g., the combined effects of relative permeability and capillary pressure analyzed in this study. Results from this study initially demonstrate that

entry pressure ($P_o$) from the capillary pressure model is the dominant control to both $CO_2$ plume distribution and pressure propagation, and entry pressure should be emphasized during reservoir evaluation and risk monitoring during CCS projects.

Results from this study also demonstrate that the trained ML model offers an alternative method for simulating $CO_2$ saturation and fluid pressure migration features across a high-dimensional parameter space. Furthermore, the new ML model represents advantages in terms of computational efficiency and run-time acceleration. For example, the physics-based simulations developed for this study required ~4000 h (~6 months) CPU time to produce 460 $CO_2$ injection simulations using the TOUGH3 code. In contrast, it takes a few hours to train the ML model to this entire dataset, and a few minutes to make predictions about thousands of combinations of reservoir parameters. In general, the trained ANN model can accelerate the $CO_2$ saturation and pressure distribution prediction process without training by at least 25,000%. In addition, the Pytorch ML library [74,76] was been shown here to result in a highly efficient workflow; the ANN model developed for this project comprises just a couple of hundred lines of python code.

In addition, the trained ML model provides an immense potential for predicting $CO_2$ migration results over an extended parameter range, which may prove beneficial for developing intuition about the outcomes of complex multi-phase flow and transport processes in the face of substantial parametric uncertainty. Moreover, the combination of ANN simulation methods and response surface analysis provides a framework for efficiently analyzing parametric uncertainty with increasingly higher dimensionality. More broadly, the trained ANN model performs well in capturing $CO_2$ saturation and pressure features during CCS and shows the capability in facilitating closer examination of larger parameter spaces with substantial gains of computational efficiency. As a result, the examination can contribute to deeper understanding in the underlying physical fundamentals of $CO_2$ saturation and pressure perturbation mechanisms. The application of this modeling approach may also provide new avenues of support for in the siting CCS projects. Furthermore, the workflow developed here for ANN model development is broadly applicable to numerous geoenergy technologies, e.g., enhanced geothermal, oilfield wastewater disposal, subsurface hydrogen storage, and nuclear waste disposal.

## 5. Conclusion

This study combines physics-based multi-phase simulations with machine learning methods to simultaneously interrogate the 3-D parameter space that governs both capillary pressure and relative permeability. The physics-based models are utilized as training input for an ANN emulator that reproduced $CO_2$ saturation and fluid pressure distribution over a wide range. The trained ANN model provides accurate prediction over a large parameter space with speedups of at least 25,000 times, in which the massive simulation ensembles can be generated in minutes comparing to several months which are typically required to run physics-based simulations with TOUGH3 codes. Once trained with the physics-based simulations, the prediction results though the ANN model provides basic insights into $CO_2$ migration physics and phenomenology.

Analyzing the fundamental parameters ($P_o$, $\lambda$, and $S_{gr}$) that govern the multi-phase $CO_2$-brine flow suggests that

(1) Capillary entry pressure ($P_o$) is the dominant parameter at the small $P_o$ range. Small $P_o$ encourages the migration of $CO_2$ saturation and fluid pressure accumulation, while large $P_o$ inhibits the migration.

(2) The effect of $\lambda$ and $S_{gr}$ increase along with the increase of $P_o$. Especially, for saturation, the effect of $S_{gr}$ increases with decreasing $\lambda$ for the large $P_o$ range. Moreover, large $\lambda$ and small $S_{gr}$ encourages the migration of $CO_2$ saturation. In contrast, for pressure, the migration is encouraged by high $S_{gr}$.

(3) With the trained ANN model, the $CO_2$ migration prediction over a large parameter space has achieved an acceleration by ~25,000%, which decreases the computational time scale of massive multi-phase fluid flow simulation ensembles from years to hours.

The analyses of different parameters from capillary pressure and relative permeability models provide a more comprehensive understanding of the $CO_2$ saturation and pressure migration mechanisms. More broadly, this artificial neural network approach could be applied to other geologic fluid systems to gain deeper insights into the complicated relationships between multi-phase fluid flow, thermodynamics, and fluid-rock interactions.

## CRediT authorship contribution statement

**Hao Wu:** Conceptualization, Methodology, Software, Validation, Formal analysis, Investigation, Resources, Data curation, Visualization, Supervision, Project administration. **Nicholas Lubbers:** Conceptualization, Software. **Hari S. Viswanathan:** Conceptualization. **Ryan M. Pollyea:** Conceptualization, Resources.

## Declaration of Competing Interest

The authors declare that they have no known competing financial interests or personal relationships that could have appeared to influence the work reported in this paper.

## Appendix A. Supplementary material

Supplementary data to this article can be found online at https://doi.org/10.1016/j.apenergy.2021.116580.

## References

[1] Metz B, Davidson O, Coninck H, Loos M, Meyer L. Carbon dioxide capture and storage: special report of the intergovernmental panel on climate change. Cambridge University Press; 2005.

[2] Michael K, Golab A, Shulakova V, Ennis-King J, Allinson G, Sharma S, et al. Geological storage of $CO_2$ in saline aquifers – a review of the experience from existing storage operations. Int J Greenhouse Gas Control 2010;4(4):659–67.

[3] Sharma SS. Determinants of carbon dioxide emissions: empirical evidence from 69 countries. Appl Energy 2011;88:376–82.

[4] Viebahn P, Vallentin D, Holler S. Prospects of carbon capture and storage (CCS) in India's power sector – an integrated assessment. Appl Energy 2014;117:62–75.

[5] Viebahn P, Vallentin D, Höller S. Prospects of carbon capture and storage (CCS) in China's power sector – an integrated assessment. Appl Energy 2015;157:229–44.

[6] Bennion B, Bachu S. Relative permeability characteristics for supercritical CO2 displacing water in a variety of potential sequestration zones in the western Canada sedimentary basin. In: Society of Petroleum Engineers Annual Technical Conference and Exhibition, Dallas, Texas; 2005.

[7] Dai Z, Middleton R, Viswanathan H, Fessenden-Rahn J, Bauman J, Pawar R, et al. An integrated framework for optimizing $CO_2$ sequestration and enhanced oil recovery. Environ Sci Technol Lett 2013;1(1):49–54.

[8] Herzog H, Golomb D, Zemba S. Feasibility, modeling and economics of sequestering power plant $CO_2$ emissions in the deep ocean. Environ Prog Sustain Energy 1991;10(1):64–74.

[9] Shi JQ, Xue Z, Durucan S. Supercritical $CO_2$ core flooding and imbibition in Tako sandstone – Influence of sub-core scale heterogeneity. Int J Greenhouse Gas Control 2011;5:75–87.

[10] Iglauer S, Paluszny A, Pentland CH, Blunt MJ. Residual $CO_2$ imaged with X-ray micro-tomography. Geophys Res Lett 2011;38:L21403.

[11] Shaffer G. Long-term effectiveness and consequences of carbon dioxide sequestration. Nat Geosci 2010;3:464–7.

[12] Jayne RS, Zhang Y, Pollyea RM. Using heat as a predictor of $CO_2$ breakthrough in highly heterogeneous reservoirs. Geophys Res Lett 2019;46(11):5879–88. https://doi.org/10.1029/2019GL083362.

[13] Wu H, Jayne RS, Pollyea RM. A parametric analysis of capillary pressure effects during geologic carbon sequestration in a sandstone reservoir. Greenhouse Gas Sci Technol 2018;00:1–14. https://doi.org/10.1002/ghg.1815.

[14] Pollyea RM. Influence of relative permeability on injection pressure and plume configuration during $CO_2$ injections in a mafic reservoir. Int J Greenhouse Gas Control 2016;46:7–17. https://doi.org/10.1016/j.ijggc.2015.12.025.

[15] Pini R, Krevor SCM, Benson SM. Capillary pressure and heterogeneity for the $CO_2$/water system in sandstone rocks at reservoir conditions. Adv Water Resour 2012;38:48–59.

[16] Pawar R, Dilmore R, Chu S, Zhang Y, Oldenburg C, Stauffer P, et al. Informing geologic $CO_2$ storage site management decisions under uncertainty: demonstration of NRAP's integrated assessment model (NRAP-IAM-CS) application. Energy Procedia 2017;114:4330–7.

[17] Ferrand LA, Celia MA. The effect of heterogeneity on the drainage capillary pressure-saturation relation. Water Resour Res 1992;28(3):859–70.

[18] Chaouche M, Rakotomalala N, Salin D, Xu B, Yortsos YC. Capillary effects in drainage in heterogeneous porous media: continuum modelling, experiments and pore network simulations. Chem Eng Sci 1994;49(15):2447–66.

[19] Ataie-Ashtiani B, Hassanizadeh SM, Celia MA. Effects of heterogeneities on capillary pressure–saturation–relative permeability relationships. J Contam Hydrol 2002;56:175–92.

[20] Arns JY, Arns CH, Sheppard AP, Sok RM, Knackstedt MA, Pinczewski WV. Relative permeability from tomographic images; effect of correlated heterogeneity. J Pet Sci Eng 2003;39(3–4):247–59.

[21] Cihan A, Birkholzer J, Trevisan L, González-Nicolás A, Illangasekare T. Investigation of representing hysteresis in macroscopic models of two-phase flow in porous media using intermediate scale experimental data. Water Resour Res 2017;53:199–221.

[22] Pruess K, García J. Multiphase flow dynamics during $CO_2$ disposal into saline aquifers. Environ Geol 2002;42:282–95.

[23] d'Amore F, Mocellin P, Vianello C, Maschio G, Bezzo F. Economic optimisation of European supply chains for $CO_2$ capture, transport and sequestration, including societal risk analysis and risk mitigation measures. Appl Energy 2018;223:401–15.

[24] Sun AY, Jeong H, González-Nicolás A, Templeton TC. Metamodeling-based approach for risk assessment and cost estimation: application to geological carbon sequestration planning. Comput Geosci 2018;113:70–80.

[25] Cody BM, Baù D, González-Nicolás A. Stochastic injection-strategy optimization for the preliminary assessment of candidate geological storage sites. Hydrogeol J 2015;23(6):1229–45.

[26] Bromhal GS, Birkholzer J, Mohaghegh SD, Sahinidis N, Wainwright H, Zhang Y, et al. Evaluation of rapid performance reservoir models for quantitative risk assessment. Energy Procedia 2014;63:3425–31.

[27] González-Nicolás A, Baù D, Alzraiee A. Detection of potential leakage pathways from geological carbon storage by fluid pressure data assimilation. Adv Water Resour 2015;86:366–84.

[28] Zhang L, Dilmore R, Namhata A, Bromhal G. Feasibility of $CO_2$ migration detection using pressure and $CO_2$ saturation monitoring above an imperfect primary seal of a geologic $CO_2$ storage formation: a numerical investigation. Comput Geosci 2018;22(3):909–23.

[29] Jayne RS, Wu H, Pollyea RM. Geologic $CO_2$ sequestration and permeability uncertainty in a highly heterogeneous reservoir. Int J Greenhouse Gas Control 2019;83:128–39. https://doi.org/10.1016/j.ijggc.2019.02.001.

[30] Yang YM, Dilmore R, Mansoor K, Carroll S, Bromhal G, Small M. Risk-based monitoring network design for geologic carbon storage sites. Energy Procedia 2017;114:4345–56.

[31] Trevisan L, Pini R, Cihan A, Birkholzer JT, Zhou Q, González-Nicolás A, et al. Imaging and quantification of spreading and trapping of carbon dioxide in saline aquifers using meter-scale laboratory experiments. Water Resour Res 2017;53:485–502.

[32] Agartan E, Trevisan L, Cihan A, Birkholzer J, Zhou Q, Illangasekare T. Experimental study on effects of geologic heterogeneity in enhancing dissolution trapping of supercritical $CO_2$. Water Resour Res 2015;51:1635–48.

[33] Zhao B, MacMinn CW, Huppert HE, Juanes R. Capillary pinning and blunting of immiscible gravity currents in porous media. Water Resour Res 2014;50:7067–81.

[34] González-Nicolás A, Baù D, Cody BM, Alzraiee A. Stochastic and global sensitivity analyses of uncertain parameters affecting the safety of geological carbon storage in saline aquifers of the Michigan Basin. Int J Greenhouse Gas Control 2015;37:99–114.

[35] Yu SY, Akervoll I, Torsaeter O, Stensen JA, Kleppe J, Midtlyng SH. History matching gas injection processes with in-situ saturation measurements and process hysteresis. In: Society of Petroleum Engineers International Oil and Gas Conference and Exhibition in China, Beijing, China; 1998.

[36] André L, Peysson Y, Azaroual M. Well injectivity during $CO_2$ storage operations in deep saline aquifers–part 2: Numerical simulations of drying, salt deposit mechanisms and role of capillary forces. Int J Greenhouse Gas Control 2014;22:301–12.

[37] Mudunuru MK, O'Malley D, Srinivasan S, Hyman JD, Sweeney MR, Frash L, et al. Physics-informed machine learning for real-time unconventional reservoir management. Assoc Adv Artif Intell 2020.

[38] DeVries PMR, Thompson TB, Meade BJ. Enabling large-scale viscoelastic calculations via neural network acceleration. Geophys Res Lett 2017;44:2662–9.

[39] Pollyea RM, Fairley JP, Podgorney RK, Mcling TL. Physical constraints on geologic $CO_2$ sequestration in low-volume basalt formations. GSA Bull 2014;126(3–4):344–51. https://doi.org/10.1130/B30874.1.

[40] Karpatne A, Ebert-Uphoff I, Ravela S, Babaie HA, Kumar V. Machine learning for the Geosciences challenges and opportunities. IEEE Trans Knowl Data Eng 2019;31(8).

[41] Lary DJ, Alavi AH, Gandomi AH, Walker AL. Machine leaning in geosciences and remote sensing. Geosci Front 2016;7:3–10.

[42] Rouet-Leduc B, Hulbert C, Lubbers N, Barros K, Humphreys CJ, Johnson PA. Machine learning predicts laboratory earthquakes. Geophys Res Lett 2017;44:9276–82.

[43] Köppel M, Franzelin F, Kröker I, Oladyshkin S, Santin G, Wittwar D, et al. Comparison of data-driven uncertainty quantification methods for a carbon dioxide storage benchmark scenario. Comput Geosci 2019;23:339–54.

[44] Karpatne A, Jiang Z, Vatsavai RR, Shekhar S, Kumar V. Monitoring land-cover changes: a machine-learning perspective. IEEE Geosci Remote Sens Mag 2016;4(2):8–21.

[45] Marjanović M, Kovačević M, Bajat B, Voženílek V. Landslide susceptibility assessment using SVM machine learning algorithm. Eng Geol 2011;123(3):225–34.

[46] Smith JS, Isayev O, Roitberg AE. ANI-1: an extensible neural network potential with DFT accuracy at force field computational cost. Chem Sci 2017;8:3192.

[47] Chen B, Harp DR, Lin Y, Keating EH, Pawar RJ. Geologic $CO_2$ sequestration monitoring design: a machine learning and uncertainty quantification based approach. Appl Energy 2018;225:332–45.

[48] Bergen KJ, Johnson PA, Maarten V, Beroza GC. Machine learning for data-driven discovery in solid earth geoscience. Science 2019;363:1299.

[49] Sun AY. Optimal carbon storage reservoir management through deep reinforcement learning. Appl Energy 2020. available online 10 August.

[50] Dahshan M, Polys NF, Jayne RS, Pollyea RM. Making sense of scientific simulation ensembles with semantic interaction. Comput Graphics Forum 2020. https://doi.org/10.1111/cgf.14029.

[51] Maniar H, Ryali S, Kulkarni MS, Abubakar A. Machine learning methods in geosciences. In: SEG international exposition and 88th annual meeting, Anaheim, California; 2018.

[52] Srinivasan S, Karra S, Hyman J, Viswanathan H, Srinivasan G. Model reduction for fractured porous media: a machine learning approach for identifying main flow pathways. Comput Geosci 2019;23:617–29.

[53] Valera M, Guo Z, Kelly P, Matz S, Cantu VA, Percus AG, et al. Machine learning for graph-based representations of three-dimensional discrete fracture networks. Comput Geosci 2018;22:695–710.

[54] Poulton MM. Neural networks as an intelligence amplification tool: a review of applications. Geophysics 2002;67(3):979–93.

[55] Walls JD, Taner MT, Guidish T, Taylor G, Dumas D, Derzhi N. North Sea reservoir characterization using rock physics, seismic attributes, and neural networks; a case history. In: SEG Technical Program Expanded Abstracts; 1999. Society of Exploration Geophysicists, p. 1572–75.

[56] Bishop CM. Neural networks for pattern recognition. Oxford Univ. Press; 1995.

[57] Hinton GE, Salakhutdinov RR. Reducing the dimensionality of data with neural networks. Science 2006;333:504–7.

[58] Li B, Zhou F, Li H, Duguid A, Que L, Xue Y, et al. Prediction of $CO_2$ leakage risk for wells in carbon sequestration fields with an optimal artificial neural network. Int J Greenhouse Gas Control 2018;68:276–86.

[59] Beucher A, Österholm P, Martinkauppi A, Edén P, Fröjdö S. Artificial neural network for acid sulfate soil mapping: application to the Sirppujoki River catchment area, south-western Finland. J Geochem Explor 2013;125:46–55.

[60] Berg S, Oedai S, Ott H. Displacement and mass transfer between saturated and unsaturated $CO_2$-brine systems in sandstone. Int J Greenhouse Gas Control 2013;12:478–92.

[61] van Genuchten MT. A closed-form equation for predicting the hydraulic conductivity of unsaturated soils. Soil Sci Soc Am J 1980;44(5):892–8.

[62] Corey A. The interrelation between gas and oil relative permeabilities. Prod Monthly 1954:38–41.

[63] Roels SM, Chatib NEL, Nicolaides C, Zitha PLJ. Capillary-driven transport of dissolved salt to the drying zone during $CO_2$ injection in homogeneous and layered porous media. Transp Porous Media 2016;111:411–24.

[64] Bachu S, Bennion B. Effects of in-situ conditions on relative permeability characteristics of $CO_2$-brine systems. Environ Geol 2008;54:1707–22.

[65] Oh J, Kim KY, Han WS, Kim T, Kim JC, Park E. Experimental and numerical study on supercritical $CO_2$/brine transport in a fractured rock: Implications of mass transfer, capillary pressure and storage capacity. Adv Water Resour 2013;62:442–53.

[66] Bennion DB, Bachu S. Dependence on temperature, pressure, and salinity of the IFT and relative permeability displacement characteristics of CO2 injected in deep saline aquifers. In: 2006 SPE Technical Conference and Exhibition. Society of Petroleum Engineers, San Antonio, TX; 2006.

[67] Benson S, Tomutsa L, Silin D, Kneafsy T. Core scale and pore scale studies of carbon dioxide migration in saline formations. In: 8th International Conference on Greenhouse Gas Control Technologies (GHGT-8), Trondheim, Norway; 2006.

[68] Bertels SP, DiCarlo DA, Blunt MJ. Measurement of aperture distribution, capillary pressure, relative permeability, and in situ saturation in a rock fracture using computed tomography scanning. Water Resour Res 2001;37:649–62.

[69] Jung Y, Pau GSH, Finsterle S, Pollyea RM. TOUGH3: A new efficient version of the TOUGH suite of multiphase flow and transport simulators. Comput Geosci 2017; 108:2–7. https://doi.org/10.1016/j.cageo.2016.09.009.

[70] Pruess K, Spycher N. ECO2N–A fluid property module for the TOUGH2 code for studies of CO2 storage in saline aquifers. Energy Convers Manage 2007;48(6): 1761–7.

[71] Valentine AP, Woodhouse JH. Approaches to automated data selection for global seismic tomography. Geophys J Int 2010;182:1001–12.

[72] Neilsen MA. Neural networks and deep learning. Determination Press; 2015. [Available at http://neuralnetworksanddeeplearning.com].

[73] Kingma DP, Ba JL. ADAM: a method for stochastic optimization. arXiv preprint arXiv:1412.6980; 2015.

[74] Paszke A, Gross S, Massa F, Lerer A, Bradbury J, Chanan G, et al. PyTorch: an imperative style, high-performance deep learning library. Adv Neural Inf Process Syst 2019;32:8024–35.

[75] Harp DR, O'Malley D, Yan B, Pawar R. On the feasibility of using physics-informed machine learning for underground reservoir pressure management. Expert Syst Appl 2021. in review.

[76] van Rossum G, Drake Jr FL. Python reference manual. Centrum voor Wiskunde en Informatica Amsterdam; 1995.